Comparison between grooved and plane aerostatic thrust bearings: static performance

Comparison between grooved and plane aerostatic thrust bearings: static performance

Guido Belforte · Federico Colombo · Terenziano Raparelli · Andrea Trivella · Vladimir Viktorov

Abstract The demand of air bearings is increasing for those applications that require precision linear movements or high-speed rotations. In particular in this paper air pads for air motion technology are studied. The paper analyses the effect of a circumferential groove machined on the pad surface on pressure distribution, air flow consumption and stiffness. Two geometries are investigated and compared: one with three supply orifices and the other with a circumferential groove as well. The static characteristics of the pads are experimentally determined with also the pressure distributions under the pads along the radial and circumferential directions. The experimental pressure distributions are compared with the simulated ones, obtained with a numerical program at the purpose developed. The numerical model considers a general formulation of the supply holes discharge coefficient that can be used also in presence of a circumferential groove.

Keywords Gas thrust bearing · Groove · Circular pad · Discharge cefficient

Nomenclature

b critical ratio
c_d discharge coefficient of supply orifices
d supply orifice diameter
d_0 insert diameter
l supply orifice length
h air clearance
h_g groove depth
r radial direction
r_g radius of supply circumference
p_a ambient absolute pressure
p_s supply absolute pressure
p_c supply orifice downstream absolute pressure q inlet mass flow rate per unit surface
q_r radial mass flow rate per unit circumf. length q_θ circumf. mass flow rate per unit radial length w_g width of the annular groove
C_s conductance of supply port
N number of supply orifices
R^0 gas constant $= 287.6$ m $^2/$s^2 K
S supply orifice cross section
T^0 absolute temperature in normal condition
δ pocket depth

θ circumferential angle
ϕ_e pad external diameter
ϕ_i pad internal diameter

1 Introduction

The fields in which gas bearings are used can be classified into two groups: high speed applications and high precision positioning systems. In the field of precision technology pneumatic pads are often used to support measuring machines, micro assembling systems and machine tool calibration and inspection systems. A peculiarity of air bearings is the very low friction and absence of stick and slip phenomenon. This allows to obtain high repeatability and high resolution. Moreover the absence of contact in the pneumatic linear guides means virtually zero wear.

The pads used in these systems can be endowed with simple supply holes [1–4], supply holes with feed pockets [5, 6] or feeding systems with microgrooves [7–12]. Other pads are provided of different systems of load compensation [13, 14] or are composed with porous materials [15–17].

In the past years gas bearings have been widely studied and in literature many experimental and theoretical studied of such components can be found [18–21]. Anyway often the numerical models used to simulate the pressure distribution in the clearance consider the discharge coefficient of the supply holes either constant [22, 23] or expressed by empirical formulas [24, 25] that are not of general validity. Other papers calculate the air flow rate through the supply holes by using CFD commercial software [6, 26–28]. The limitation of this approach is that it needs an exact definition of the supply holes geometry, that is practically impossible, because the results are very sensi-tive to geometric parameters. For example in [27] i t is shown that the presence of a fillet or a chamfer between the supply hole wall and the pad surface influences a lot the pressure distribution near the supply hole. For these motivations it is necessary in any case to identify experimentally the supply holes discharge coefficients.

In paper [29] it was proposed an empirical formula for the supply holes discharge coefficient as a function of geometric parameters and Reynolds number. The formula is applicable to inherently compensated bearings with simple and pocketed supply holes. It shows that the discharge coefficient varies significantly for subsonic flow condition, especially for low Reynolds numbers.

In the present study the static experimental performance of two circular pneumatic pads are compared with numerical results obtained with this formulation for the discharge coefficient. The aim of the paper is to show the validity of the formulation also in presence of a circumferential groove of width greater than the supply hole diameter. The first pad presents simple orifices, the second one is endowed of a pocket and a circumferential groove too.

2 Pads under test

Two flat pad circular air bearings are considered. They have external diameter 40 mm and present three supply orifices of diameter $d = 0.3$ mm equally spaced on a circumference of diameter 25 mm. In the first one (pad 1) the orifices are drilled on inserts of diameter d_0 mounted in the pad without creating any pockets. On the second pad (pad 2) a circular groove of depth $h_g = 10$ μm and width $w_g = 0.7$ mm is machined on the same circumference of the supply orifices. In this pad the inserts are mounted in order to generate a pocket of depth $\delta = 10$ μm. In this way the circumferential groove, that is machined on the pad surface and not on the inserts, is not interrupted.

Figure 1 shows the sketch of the two pads, that are provided with a central vented camera of diameter 10 mm and depth 5 mm. Each supply hole is numbered in anticlockwise direction.

In the sketch the pocket and the groove depths are increased in order to appreciate them. The nominal rugosity of the pads surface is Ra = 0.4 μm.

The photo of the two pads is shown in Fig. 2.

The supply orifices diameters were checked with a microscope. The 100X enlargement of Fig. 3 is obtained with a system with lenses and optical fibres. In Table 1 the measured diameters of the supply orifices are collected, with also the errors between nominal and measured values.

The groove depth and width were measured by a rugosimeter and were verified to be respectively 9 μm and 800 μm. In Fig. 4 is shown the groove profile.

The mean rugosity is Ra = 0.455 μm for pad 1 and Ra = 0.4 μm for pad 2.

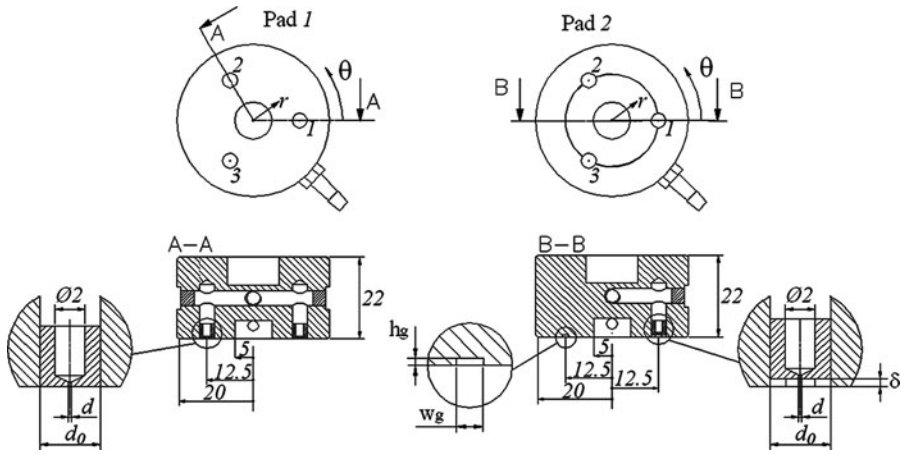

Fig. 1 Sketch of the pads

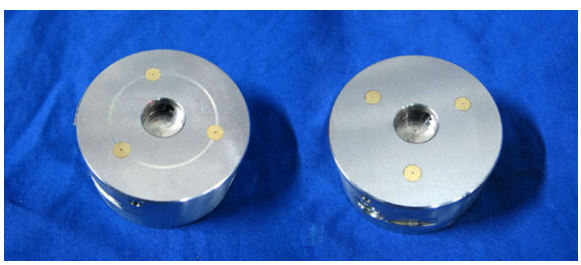

Fig. 2 Photo of the pads

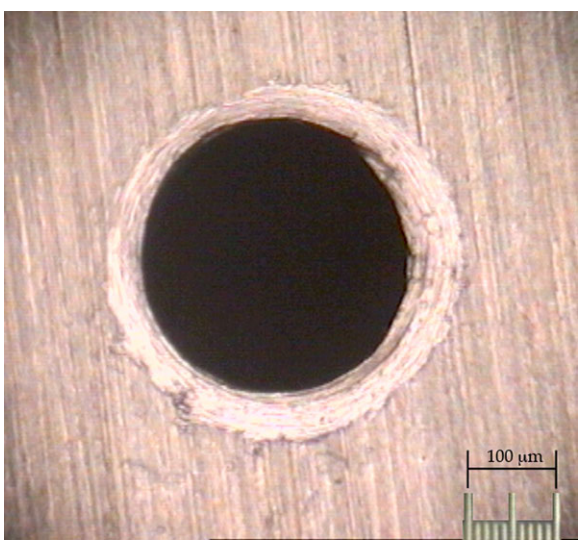

Fig. 3 Enlargement of supply orifice 3, pad 1

Table 1 Measured values of supply orifices diameter

Pad	Orifice	Nominal orifice diameter (mm)	Measured diameter (mm)	Error %
1	1	0.3	0.312	3.8
1	2	0.3	0.313	4.3
1	3	0.3	0.315	4.8
2	1	0.3	0.320	6
2	2	0.3	0.312	4
2	3	0.3	0.300	0

3 Numerical model

The pressure distribution under the pads is calculated by solving the Reynolds equation for compressible flu-ids expressed in polar coordinates (1)

$$\frac{1}{r}\frac{\partial}{\partial r}\left(rh^3\frac{\partial p^2}{\partial r}\right)+\frac{1}{r^2}\frac{\partial}{\partial \vartheta}\left(h^3\frac{\partial p^2}{\partial \vartheta}\right)+24\mu R^0T^0q=24\mu\frac{\partial(ph)}{\partial t}. \quad (1)$$

The Reynolds equation is discretized with finite difference technique considering a $n \times m$ polar grid and then it is solved with Euler explicit method. For each grid point the pressure is calculated by (2)

$$p_{i,j}^{t+1}=p_{i,j}^{t}+\frac{\Delta t}{24\mu h_{i,j}}\left[\frac{h^3}{r}\frac{p_{i+1,j}^2-p_{i-1,j}^2}{2\Delta r}+\frac{h^3}{\Delta r^2}\left(p_{i+1,j}^2-2p_{i,j}^2+p_{i-1,j}^2\right)\right.$$

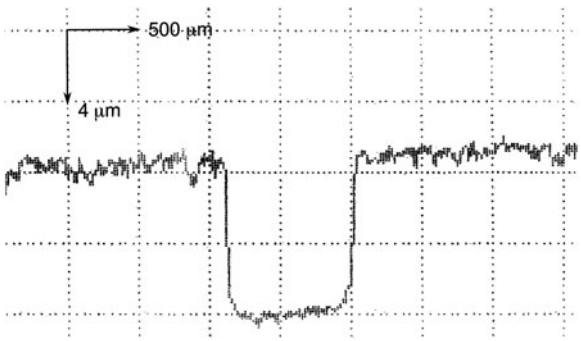

Fig. 4 Groove profile measured with a rugosimeter

$$+\frac{h_{i,j}^3}{(r\Delta\vartheta)^2}\left(p_{i,j+1}^2-2p_{i,j}^2+p_{i,j-1}^2\right)+24\mu R^0T^0q_{i,j}\Bigg]. \tag{2}$$

The air clearance in correspondence of the i-th node along the radial direction and the j-th node along the circumferential direction is defined as

$$h_{i,j}=\begin{cases}h+h_{\mathrm{g}}, & r=r_{\mathrm{g}},\\ h, & r\neq r_{\mathrm{g}},\end{cases} \tag{3}$$

depending if the node is situated in correspondence of the circumferential groove or not.

Similarly the inlet mass flow rate per unit surface $q_{i,j}$ is considered zero everywhere except in correspondence of the supply orifices.

Equation (2) is used with a circumferential groove of width equal to the radial mesh size dr. In fact the radial flow is calculated with clearance h, while the circumferential flow with $h_{i,j}$. Figure 5 shows the finite difference grid and the control volume to which the continuity equation of mass flow rate is applied in correspondence of the groove. As the groove width is negligible with respect to the pad size the control volume is centered in the groove and its radial dimension is equal to the groove width. In this way radial pressure gradients inside the groove are not taken into account. Equation (2) can be extended to the case in which the groove width is greater than the radial mesh size. In this case inside the groove both the radial and the cir-cumferential flows must be calculated with $h + h_{\mathrm{g}}$. The clearance derivative of h in correspondence of the clearance discontinuity is not taken into account, be-cause it doesn't influence the air flow rate along the radial direction q_{r}.

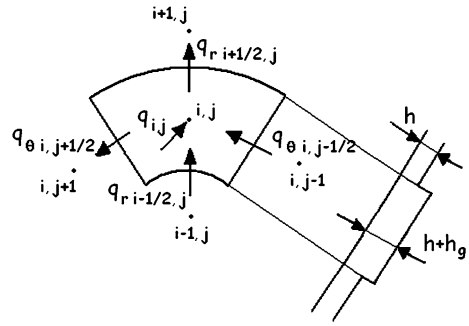

Fig. 5 Control volume to which the continuity equation is applied

The mass flow rate that enters in the control volume $h\cdot rd\vartheta\cdot dr$ is $G_{i,j}=q_{i,j}\,(rdrd\vartheta)$. $G_{i,j}$ is given by (4) and depends on the pressure drop through the orifice, from the supply pressure p_{s} to the downstream pres-sure p_{c}. The conductance is expressed by (5)

$$G_{i,j}=\begin{cases}C_{\mathrm{s}}k_T\rho_N p_{\mathrm{s}}, & \text{if } 0<\frac{p_{\mathrm{c}}}{p_{\mathrm{s}}}<b,\\ C_{\mathrm{s}}k_T\rho_N p_{\mathrm{s}}\sqrt{1-(\frac{\frac{p_{\mathrm{c}}}{p_{\mathrm{s}}}-b}{1-b})^2}, & \text{if } \frac{p_{\mathrm{c}}}{p_{\mathrm{s}}}>b,\end{cases} \tag{4}$$

$$C_{\mathrm{s}}=0.686\frac{c_{\mathrm{d}}S}{\rho_N\sqrt{R^0T^0}}. \tag{5}$$

The discharge coefficient c_{d} is calculated using a formula obtained from experimental identification [29]. The interpolating formula (6) considers the local clear-ance under the supply orifice and its diameter d. The local clearance is $h + h_{\mathrm{g}}$ in the groove and $h + \delta$ in correspondence of the pocket. The discharge flow de-pends also on Reynolds number Re, calculated by (7)

$$c_{\mathrm{d}}=0.85\left(1-e^{-8.2\frac{h+\delta}{d}}\right)\cdot\left(1-e^{-0.001Re\frac{h+\delta}{h+4\delta}}\right), \tag{6}$$

$$Re=\frac{4G_{i,j}}{\pi d\mu}. \tag{7}$$

The pads are simulated considering one of the N sectors of the pad (between $\theta=0$ and $\theta=2\pi/N$), where N is in general the number of supply orifices equally distributed in the supply circumference. The resulting pressure distribution is extrapolated on the entire surface considering the polar symmetry.

The boundary conditions used are the following:

- $p=p_{\mathrm{a}}$ at the internal and external radius;
- periodicity at $\theta=0$ and $\theta=2\pi/N$;
- mass flow rate through the supply orifices calculated with (4).

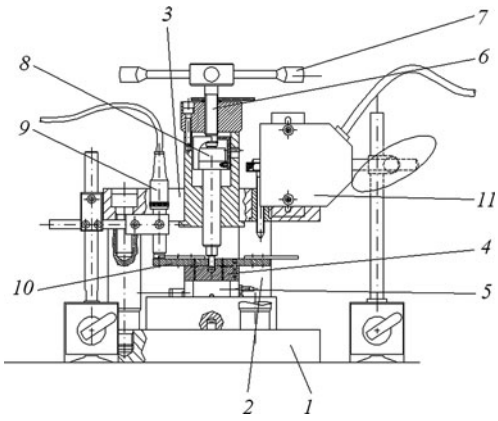

Fig. 6 Sketch of the test bench

The time transient from the initial condition of ambient pressure everywhere till the steady solution is calculated considering h time-invariant.

4 Test bench

The static pressure distributions of the pads along the radial and circumferential directions were experimentally determined on the test bench of Fig. 6.

The set-up frame consists of a base (1), three columns (2) and a crossmember (3). The air gap h is established between the pad under test (4) and the stationary bearing member (5). The pad (4) can be moved vertically by means of screw (6) and handwheel (7) when supply air is provided. The force on the pad is monitored by the load cell (8). The air gap height is monitored by 3 inductive transducers (9) that face the disk (10) screwed to the pad. A laser beam (11) is used to calibrate *in loco* the inductive sensors. These last are mounted at 120° facing a disk screwed to the pad. The clearance is obtained as the average displacement value from the zero point. A measuring hole of diameter 0.2 mm is provided in the stationary bearing member (5) and connected to a pressure transducer: in this way the pressure in the air gap in correspondence to the measuring hole is measured. The pressure distribution can be measured both in radial and circumferential directions. In the first case the stationary bearing member is moved along the radial direction. By moving the measuring hole with respect to the pad it is possible to measure the radial pressure distribution under the pad. The motion is provided by a screw and is measured by a displacement transducer.

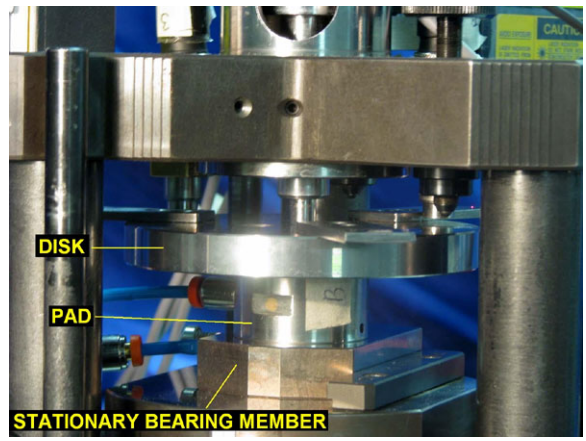

Fig. 7 Enlargement of the pad under test

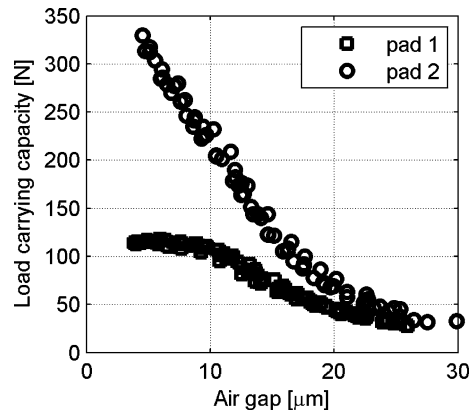

Fig. 8 Static load capacity vs clearance h characteristics, $p_s = 0.6$ MPa; comparison between pad 1 and pad 2

In the second case the base is rotated on a central pivot while the pad is maintained fixed so that the measuring hole moves along a circumference centered with the pad.

The photo of Fig. 7 shows the enlargement of the pad during the test. The stationary bearing member and the disk on which the displacement transducers are faced are visible.

5 Experimental results

The static characteristics of load carrying capacity and stiffness of the pads, shown in Figs. 8 and 9, and the mass flow rates, visible in Fig. 10, were measured sev-eral times in order to verify their repeatability. The ab-solute supply pressure is $p_s = 0.6$ M P a .

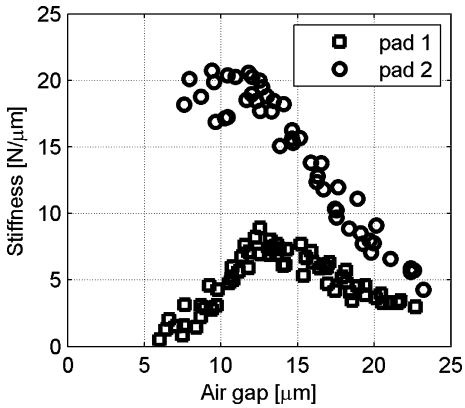

Fig. 9 Static stiffness vs clearance h characteristics, $p_s = 0.6$ MPa; comparison between pad 1 and pad 2

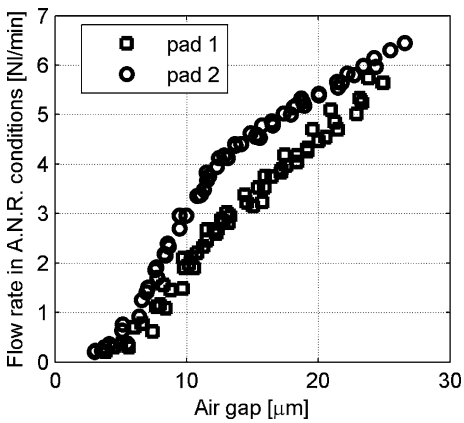

Fig. 10 Air mass flow vs clearance h, $p_s = 0.6$ MPa; comparison between pad 1 and pad 2

Pad 2 has a load carrying capacity greater than pad 1 and this is more evident at low clearance, where stiffness is much higher. It is interesting to notice that in case of groove presence the pad continues to increase its load carrying capacity at low clearance without presenting a local maximum, while this last is visible in case without groove. The difference of air flow rate consumption between the two pads is less evident than the load capacity or the stiffness.

The static radial and circumferential pressure distributions (see Figs. 11 and 12) are measured with air clearance $h = 10$ and 15 μm. Several tests have been carried out in order to verify the repeatability. The radial distributions are measured along different directions: at $\theta = 0°$, in correspondence of the supply orifices, and in the middle plane between two supply orifices ($\theta = 60°$). The circumferential distributions are

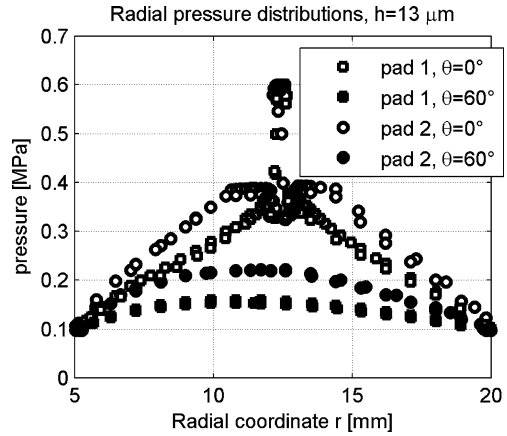

Fig. 11 Radial pressure distributions with $h = 13$ μm and $p_s = 0.6$ MPa; comparison between pad 1 and pad 2

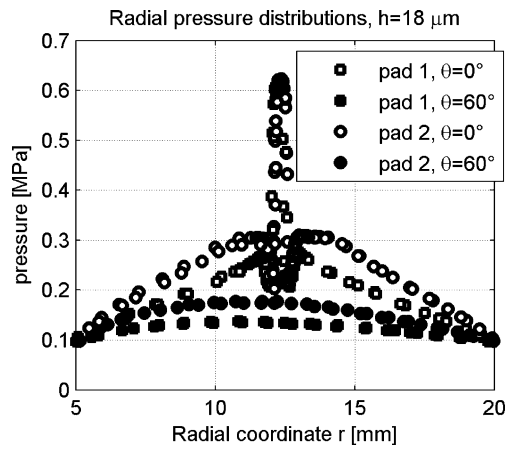

Fig. 12 Radial pressure distributions with $h = 18$ μm and $p_s = 0.6$ MPa; comparison between pad 1 and pad 2

measured in correspondence of the supply circumference.

Considering the radial pressure distribution, Figs. 11 and 12 show that the pressure in the pocket is almost constant. Moving from the supply orifice, the pressure first gradually drops to a minimum local value and then increases to a maximum local value. From this point the flow becomes purely viscous.

In circumferential direction (see Figs. 13 and 14) the pressure with pad 2 slightly decreases moving from the supply orifice, but less than with pad 1. The average pressure under the pad increases in presence of the groove.

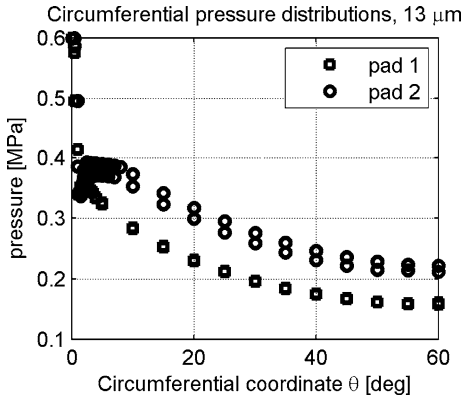

Fig. 13 Circumferential pressure distributions with $h = 13$ μm; comparison between pad 1 and pad 2

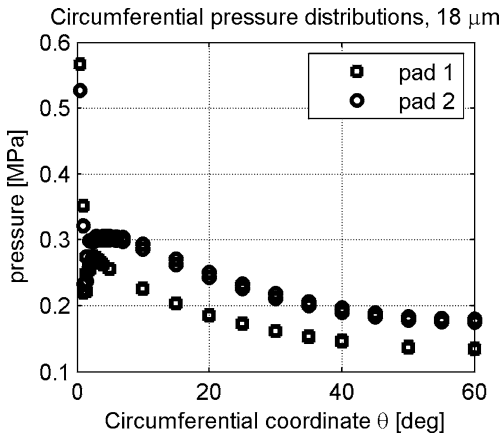

Fig. 14 Circumferential pressure distributions with $h = 18$ μm; comparison between pad 1 and pad 2

Table 2 Values of the discharge coefficients used in numerical simulations

	d [mm]	h [μm]	h_g [μm]	c_d
Pad 1	0.3	13	0	0.1
	0.3	18	0	0.21
Pad 2	0.3	13	9	0.3
	0.3	18	9	0.37

6 Numerical results and comparison

A grid of 19 radial equispaced nodes and 32 circumferential nodes (from $\theta = 0$ to $\theta = 120°$) is used. This grid presents an almost square element in correspondence of the average radius.

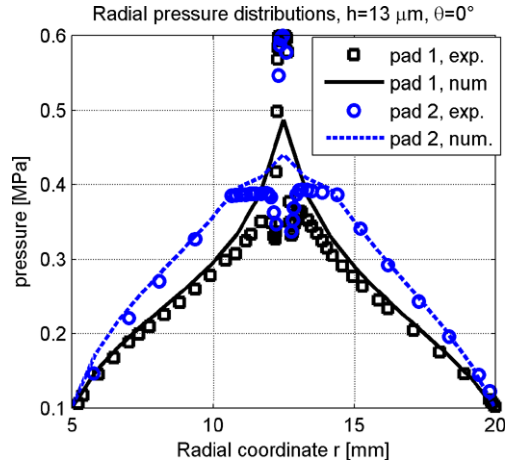

Fig. 15 Radial pressure distributions at $\theta = 0°$ with $h = 13$ μm: comparison between experimental and numerical results

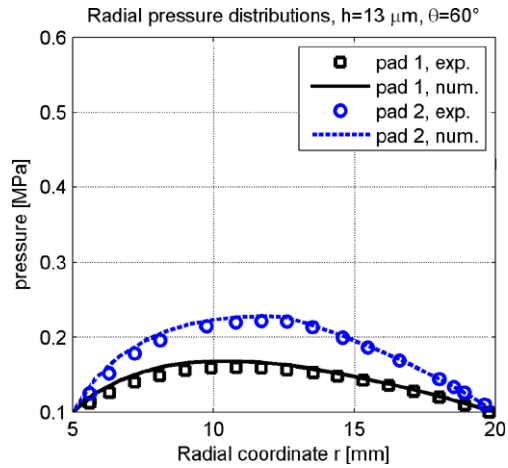

Fig. 16 Radial pressure distributions at $\theta = 60°$ with $h = 13$ μm: comparison between experimental and numerical results

The values of the discharge coefficients calculated with formula (6) overestimate the experimental pressure distribution. The values of c_d introduced in the model and shown in Table 2 are lower but anyway compatible with the dispersion of the experimental values that the formula interpolates [29].

The experimental and the numerically obtained pressure distributions are compared in Figs. 15–18. The numerical pressure distributions approximate the real pressure distributions everywhere except near the supply orifices, where the hypotheses of Reynolds equation are not satisfied.

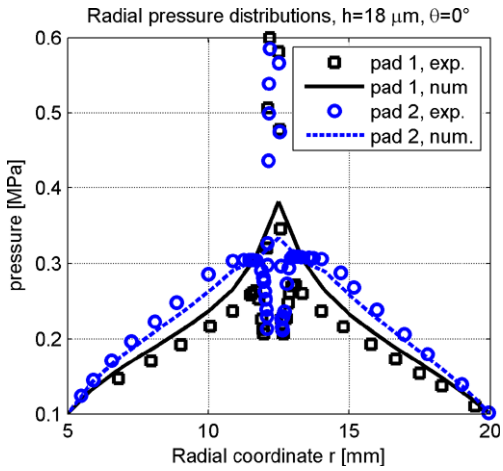

Fig. 17 Radial pressure distributions at $\theta = 0°$ with $h = 18$ μm: comparison between experimental and numerical results

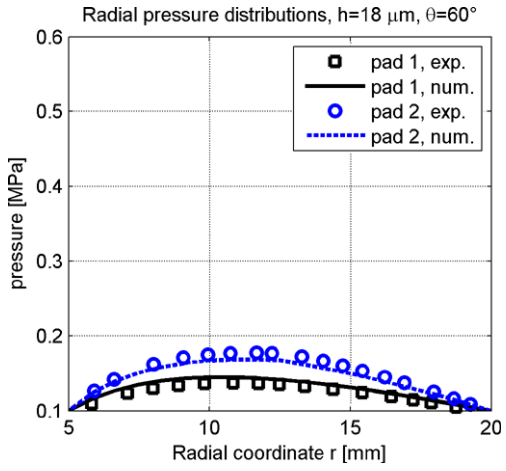

Fig. 18 Radial pressure distributions at $\theta = 0°$ with $h = 18$ μm: comparison between experimental and numerical results

Considering the radial pressure distributions with $\theta = 0°$ (Figs. 15 and 17) numerical and experimental results are in good accordance with $h = 13$ μm, while with $h = 18$ μm the discordance is more appreciable. The difference is not high, considering the high sensitivity of the pressure distribution to the value of the air clearance imposed.

This demonstrates the validity of (6) also with a groove of width greater than the supply hole diameter. In case the supply hole diameter has approximately the same value than the groove width, formulation (6) should be verified.

In all cases the comparisons in the middle plane be-tween two supply orifices ($\theta = 60°$, see Figs. 16 18) are good because in this plane the pressure distribution is less sensitive to the values of h and c_d.

7 Conclusions

The following conclusions can be stated:

- Numerical pressure distributions obtained with formulation (6) for the discharge coefficient are in accordance with the experimental ones both in case of simple holes, both with pocketed holes and circumferential groove;
- The groove presence increases the load carrying capacity and the stiffness of the pad, especially at low clearance, where the air flow increases not so much;
- With high clearances the difference of the load capacity and stiffness between pad 1 and 2 decreases, therefore the groove presence is more advantageous especially at low clearances;
- The difference of air flow between the pads is not so evident at low clearance and at high clearance, where the groove effect is almost negligible;
- The groove also avoids the effect of negative stiffness that sometimes can be experienced in pads without groove for very low clearances;
- Future interesting investigations on this topic will verify formulation (6) in cases with groove but without pocket and with a groove width approximately equal or lower than the supply hole diameter.

Acknowledgements This work was supported by MIUR: PRIN project: "Study and development of gas bearings for ultra high speed electrospindle", 2006 and FIRB project "Enabling technologies for multitasking high precision machining of microparts", 2007.

References

1. Poupard H, Drouin G (1973) Theoretical and experimental pressure distribution in supersonic domain for an inherently compensated circular thrust bearing. J Lubr Technol 95(3):217–221
2. Kazimierski Z, Trojnarski J (1980) Investigations of externally pressurized gas bearings with different feeding systems. J Lubr Technol 102(1):59–64
3. Al-Bender F, Brussel HV (1992) Symmetric radial laminar channel flow with particular reference to aerostatic bearings. J Tribol 114(7):630–636
4. Al-Bender F, Brussel HV (1992) Tilt characteristics of circular centrally fed aerostatic bearings. Tribol Int 25:189–197

5. Stout KJ, El-Ashkar S, Ghasi V, Tawfik M (1993) Theoretical analysis of two configurations of aerostatic flat pad bearings using pocketed orifice restrictors. Tribol Int 26:265–273
6. Li Y, Ding H (2007) Influence of geometrical parameters of aerostatic thrust bearing with pocketed orifice-type restrictor on its performance. Tribol Int 40:1120–1126
7. Nakamura T, Yoshimoto S (1996) Static tilt characteristics of aerostatic rectangular double-pad thrust bearings with compound restrictors. Tribol Int 29(2):145–152
8. Yoshimoto S, Tamura J, Nakamura T (1999) Dynamic tilt characteristics of aerostatic rectangular double-pad thrust bearings with compound restrictors. Tribol Int 32:731–738
9. Chen MF, Chen YP, Lin CD (2002) Research on the arc type aerostatic bearing for a PCB drilling station. Tribol Int 35:235–243
10. Chen MF, Lin YT (2002) Static behavior and dynamic stability analysis of grooved rectangular aerostatic thrust bearings by modified resistance network method. Tribol Int 35:329–338
11. Hashimoto H, Namba T (2009) Optimization of groove geometry for a thrust air bearing according to various objective functions. J Tribol 131:704–710
12. Chen MF, Huang WL, Chen YP (2010) Design of the aerostatic linear guideway with a passive disk-spring compensator for PCB drilling machine. Tribol Int 43:395–403
13. Holster PL, Jacobs JAH (1987) Theoretical analysis and experimental verification on the static properties of externally pressurized air bearing pads with load compensation. Tribol Int 20:276–289
14. Tawfik M, Stout KJ (1989) The design of high efficiency flat pad aerostatic bearings using laminar restrictions. Tribol Int 22:273–281
15. Yoshimoto S, Kohno K (2001) Static and dynamic characteristics of aerostatic circular porous thrust bearings. J Tribol 123:501–508
16. Plante J, Vogan J, El-Aguizy T, Slocum AH (2005) A design model for circular porous air bearings using the 1D generalized flow method. Precis Eng 29:336–346
17. Ng SW, Widdowson GP, Yao S (2005) Characteristics estimation of porous air bearing. In: Proceedings of the COMSOL multiphysics user's conference, Stockholm
18. Gross WA (1962) Gas film lubrication. Wiley, New York
19. Mori H, Miyamatsu Y (1969) Theoretical flow-models for externally pressurized gas bearings. J Lubr Technol 91(1):181–193
20. Fourka M, Tian Y, Bonis M (1996) Prediction of the stability of air thrust bearing by numerical, analytical and experimental methods. Wear 198:1–6
21. Kassab SZ, Noureldeen EM, Shawky A (1997) Effects of operating conditions and supply hole diameter on the performance of a rectangular aerostatic bearing. Tribol Int 30(7):533–545
22. Lund JW (1964) The hydrostatic gas journal bearing with journal rotation and vibration. J Basic Eng 86:328–336
23. Bryant MR et al (1986) A design methodology for obtaining infinite stiffness in an aerostatic thrust bearing. J Mech Transm Autom Des 108:448–456
24. Elrod HG, Glanfield GH (1971) Computer procedures for the design of flexibly mounted, externally pressurized, gas lubricated journal bearing. In: Gas bearing symposium, University of Southampton, pp 22.1–22.37
25. Kazimierski Z, Trojnarski J (1980) Investigation of externally pressurized gas bearing with different feeding systems. J Lubr Technol 102:59–64
26. Renn J, Hsiao C (2004) Experimental and CFD study on the mass flow-rate characteristic of gas through orifice-type restrictor in aerostatic bearings. Tribol Int 37:309–315
27. Belforte G et al (2006) Numerical analysis on the supply hole discharge coefficient in aerostatic bearings. In: International conference on tribology AITC-AIT 2006, 20–22 September, Parma, Italy
28. Neves MT, Schwarz AV, Menon GJ (2010) Discharge coefficient influence on the performance of aerostatic journal bearings. Tribol Int 43:746–751
29. Belforte G, Raparelli T, Viktorov V, Trivella A (2007) Discharge coefficients of orifice-type restrictor for aerostatic bearings. Tribol Int 40:512–521